

Nanostructured three-dimensional Reduced Graphene Oxide-Mn₃O₄ Architectures with High Conductivity and Bacteria Affinity for Highly Efficient Microbial Electrocatalysis

Genping Yi^{1,2,a}, Difan Fang^{1,2,a}, Liming Yang^{1,2,*}, Ziwen Chang^{1,2}, Yufa Feng^{1,2}, Wenbin Hu^{1,2},
Yanni Geng^{1,2}, Guangzhen Liu

¹ National-Local Joint Engineering Research Center of Heavy Metals Pollutants Control and Resource Utilization, Nanchang Hangkong University, Nanchang 330063, P. R. China

² Key Laboratory of Jiangxi Province for Persistent Pollutants Control and Resources Recycle, Nanchang Hangkong University, Nanchang 330063, P. R. China

*E-mail: yangliming0809185@126.com

^aGenping Yi and Difan Fang contributed equally to this work.

Received: 30 May 2020 / Accepted: 11 July 2020 / Published: 10 August 2020

Bioelectrochemical system (BES) exhibits great potential for the wastewater treatment, which can achieve the energy storage simultaneously. However, the application of BES is limited due to the interior structure and composition of electrode materials. Here, a hybrid nano-structure reduced graphene oxide-Mn₃O₄ (rGO@Mn₃O₄) electrode was obtained through one-step electrodeposition method, and utilized to enhance the performance of *Geobacter sulfurreducens* inoculated BES. The hierarchical rGO@Mn₃O₄ is equipped with open porous and higher surface roughness, which are favorable for the microbial colonization. And the electron transport from exoelectrogens to the electrode facilitated by the three-dimensional interconnecting conductive scaffold. Further, the rGO@Mn₃O₄ electrode realized the maximum current density in a three-electrode setup reached 0.0376 mA cm⁻² with high loading, which is 3.03-fold higher than that of a bare rGO (0.0124 mA cm⁻²). The great performance is attributed to the proper pore size distribution and the “rose”-like porous structure Mn₃O₄ particles coating on the surface of the rGO sheets network. This work reveals a synergistic effect in pore structure and surface chemistry design to promote bioelectrocatalysis in BESs.

Keywords: Graphene; Manganic oxide; Bioelectrochemical systems; Interface tailoring; Electron transfer; Microbial colonization

1. INTRODUCTION

With the rapid development of industrialization, severe environmental issues are emerging due to a large amount of organic and inorganic pollutants on the global scale [1-3]. The shortage of non-

renewable energy is the driving forces for the sustainable treatment and utilization/valorization of the earth resources [4-6]. Bioelectrochemical systems (BESs) are ideal platforms that employ microbes as catalysts to oxidize organic contaminants for electricity harvest, and simultaneous sewage treatment and energy recovery [7-9]. To increase the electricity production, extensive efforts have been implemented in electrochemically active microorganisms, bioelectrochemical reactor design, and bioelectrode materials [10, 11]. The bioelectrodes (bioanode and/or biocathode) are the core components that determine the cost and system performance. Extensive studies have been conducted to construct electrodes to improve the performance of BESs. According previous studies, there are various bioelectrode materials, such as fiber-based, particle-based, nonporous bulk and monolithic porous electrodes [12]. Although great achievements have been realized, insufficient biomass concentration, inferior electron transfer and weak microbial affinity have limited their practical applications of BESs. Herein, further improvement is required to comprehensively promote the performance of electricity generation through rational construction of more efficient electrode materials.

Extensive researches have been carried out on the exploitation of carbon-based hybrid materials as electrode materials in BES, for the excellent conductivity, large surface area and satisfactory porous structure [13]. However, the development of carbon-based electrodes with high microbial recombination and high efficiency of extracellular electron transfer (EET) has become the challenge [14, 15]. rGO exhibits favorable biocompatibility as a promising bioelectrode material, which is equipped with high specific surface area, large pore size and excellent electrical conductivity [16-20]. Therefore, rGO is considered to improve the power density of BES. Nevertheless, the strong π - π interaction between the rGO sheets leads to an irreversible agglomeration of these sheet layers during the chemical reduction [21, 22]. The strong hydrophobicity on the rGO surface could also hinder the adhesion and growth of bacterial, causing the reactants to proliferate poorly [23-25]. A feasible to solve the problems is to coat the transition metal oxide on the rGO electrodes, which has been proved to shuttle electrons through the redox reaction of metal oxide, promoting the adhesion of bacteria and EET [26]. Recently, manganese oxide (MnO_2) has received widely attention in BESs for the high theoretical capacitance, excellent biocompatibility and non-toxicity [27]. And the MnO_2 coated felt electrode enable increasing the power output of the microbial catalyzed electrochemical systems (MCEs) by approximately 24.7%, compare with the carbon felt electrode [28]. Nevertheless, because of the poor electroconductibility, the MnO_2 particles may act as the physical barrier for electron transfer from bacteria to the carbon electrode, when the bacteria grow on the surface of the MnO_2 -carbon electrode. In addition, the MnO_2 particles have a strong tendency to precipitate or solidify on the carbon electrode surface during the synthesis process, which brings about the reduction of the electrode surface area, restricting bacterial attachment [29, 30]. Other manganese oxides such as Mn_3O_4 also exhibits remarkable properties, with the highly active, environment friendly and easily accessible etc [31]. Although Mn_3O_4 gets well-exploited for supercapacitor and electrocatalysis, only a few papers described their applications in BESs [32-35]. Consequently, the combination of Mn_3O_4 with rGO to upgrade the composition structure and surface function of the electrodes, which might enhance the conductivity and bio-attachment for the electrodes, showing great significance in promoting the performance of the microbial catalysis.

In this work, we adopt the rGO as the support network for the Mn_3O_4 particles, to obtain a hierarchically nanostructured rGO@ Mn_3O_4 hybrid electrode via one-step electrodeposition, to fulfill the

remarkable electrical conductivity and outstanding adhesion of microbial for BESs. The purposes of this study were to (i) enhance the electrode conductivity and the electron transmission rate; and (ii) improve the microbial affinity by increasing the biocompatibility of Mn_3O_4 particles layered material.

2. EXPERIMENTAL SECTION

2.1 Chemicals and materials

Potassium permanganate (KMnO_4), lithium perchlorate (LiClO_4) and other chemicals were commercially available analytical grade reagents (Beijing Chemical Reagent Co., Ltd., China), and used directly without further purification. Ultrapure water ($18.2 \text{ M}\Omega\text{-cm}$ at 25°C) was obtained using a Milli-Q/Millipore water purification system.

2.2 Preparation of $\text{rGO@Mn}_3\text{O}_4$ electrode

Graphite oxide was prepared by using a previously-reported improved method [36]. The graphite oxide powder was exfoliated in a 0.1 M LiClO_4 solution by ultrasonication for 3 h to form a 0.5 g L^{-1} graphene oxide (GO) colloidal suspension [37]. KMnO_4 was added into the above GO suspension at a volume ratio of $V_{\text{KMnO}_4}:V_{\text{GO}} = 1:500$. Then, cyclic voltammetric electrodeposition was conducted using a three-electrode system using a CHI 660C electrochemical workstation: a glassy carbon electrode (GCE, 4 mm in diameter, 0.1256 cm^2) as the working electrode, a saturated Ag/AgCl electrode as the reference electrode, and a Pt mesh (1.0 cm^2 geometric area) as the counter electrode. The scan range was between -1.4 V and 0.6 V at a scan rate of 50 mV s^{-1} . After the electrodeposition, the electrode was rinsed with ultrapure water and dried at room temperature. For a comparison, using the same method, the pure rGO film and pure Mn_3O_4 particles were obtained from 0.5 g L^{-1} GO and LiClO_4 solution containing KMnO_4 ($V_{\text{KMnO}_4}:V_{\text{LiClO}_4} = 1:500$), respectively.

2.3 Preparation of biofilm electrode

Geobacter sulfurreducens PCA (DSM 12127) was used as the electrochemically active bacteria, which was pre-cultured in PCA standard medium according to previous work [38, 39]. Eight identical GCEs (4.0 mm in diameter) separately served as working electrodes, which shared one saturated Ag/AgCl reference electrode and one Pt mesh (1.0 cm^2 in geometric area) as the counter electrode. The activated *Geobacter* suspensions with optical density of 0.3 to 0.5 at 600 nm were then added into the electrochemical cell containing sterilized growth medium (PCA standard medium but without fumarate), which was subsequently flushed with N_2/CO_2 (80:20) for 30 min. Sodium acetate (1.0 g L^{-1}) was added and served as carbon source. For bacterial biofilm growth, the working electrodes ($\text{rGO@Mn}_3\text{O}_4$, rGO and bare GCE) were poised at $0 \text{ V vs. saturated Ag/AgCl}$ electrode, and the current was recorded with the time prolonging.

2.4 Physical characterization

The morphologies of the electrodes and biofilms were characterized by field emission scanning electron microscopy (SEM, Hitachi, SU8000) and transmission electron microscopy (TEM, FEI Tecnai G² F30 S-TWIN) equipped with an energy dispersive X-ray spectrometer (EDX). For SEM characterization of the biofilm, the obtained bioelectrodes were fixed for 2 h in 2.5% glutaraldehyde, washed three times with M9 buffer solution, dehydrated in increasing concentrations of ethanol solution (25, 50, 75, 85, 95, and 100%), and then coated with Au prior to the SEM observation. X-ray diffraction (XRD) patterns were performed on an X-ray diffractometer (Bruker D8 Advance, Germany) using Cu K α radiation ($\lambda = 0.15406$ nm) at a power of 40 keV and 3×30 mA. Raman spectra were recorded from 500 to 3500 cm^{-1} using an Advantage 200A Raman spectrometer with a 632.8 nm laser (Company name, country). N₂ adsorption-desorption isotherms were obtained at 77 K with Micromeritics TriStar II 3020 (USA) after dehydration under vacuum at 473 K for 4 h. The meso- and micro-pore size distribution was analyzed according to the Barrett-Joyner-Halenda (BJH) adsorption model, and the macro-pore size was determined using mercury porosimetry.

2.5 Electrochemical measurements

Electrochemical measurements were performed on a standard three-electrode system using an electrochemical workstation (CHI 660C). Bare GCE, rGO and rGO@Mn₃O₄ were used as the working electrode, and Pt mesh (1.0 cm² in geometric area) and saturated Ag/AgCl electrode were used as the counter electrode and the reference electrode, respectively. Cyclic voltammograms (CVs) were performed from -0.4 V to 1.0 V in N₂-saturated 1.0 M KCl solution at a scan rate of 1.0 mV s⁻¹. Electrochemical impedance spectra (EIS) were recorded by applying an AC voltage with 5.0 mV amplitude over a frequency range of 0.01 Hz to 100000 Hz at the open circuit potential. Linear cyclic voltammetry (LSV) curves for rGO@Mn₃O₄, rGO and bare GCE bioelectrodes were obtained from -0.8 V to 0.8 V at a scan rate of 1.0 mV s⁻¹.

3. RESULTS AND DISCUSSION

3.1 rGO@Mn₃O₄ synthesis and morphological characterization

The rGO@Mn₃O₄ hybrid electrode was synthesized through a simple one-step electrodeposition technique in a mixture of rGO suspension and KMnO₄ liquid. Electrodeposition as a green, simple and fast technology, which is suitable for synthesizing "clean" non-bonded electrode. During the electrochemical synthesis, the GO was electroreduced to rGO, then polymerized with manganese and deposited on the electrode, the CV was adopted for the rGO@Mn₃O₄ hybrid. Figure 1c and d are the SEM images of the hybrid rGO@Mn₃O₄ and electrodeposited CV curves are shown in Figure S1b. As shown in Figure 1c, the case of rGO@Mn₃O₄ present a three-dimensional (3D) porous structure, facilitating the formation of a conductive network. The Mn₃O₄ particles coating rGO are microspheres

in the “rose”-like structure consists of interconnected ultrathin nanosheets from the enlarge Figure 1d. And the different pore structures are formed from the morphology of Mn_3O_4 particles, which is conducive to the adhesion of microbial. These features enable the $\text{rGO@Mn}_3\text{O}_4$ electrode to obtain greater roughness of surface and more active sites with surface biocompatibility during the redox reactions, thereby improving the electron transfer rate and electrode property of BESs. And the individual Mn_3O_4 was also prepared through the same CV electrodeposition pathway Figure S1a. On contrast, the Mn_3O_4 particles aggregate to form separate clusters are observed, severely concealing the sites of microbial binding from the Figure 1a and b. The Figure 1b also shows the Mn_3O_4 particles in the “rose”-like structure. However, the “petals” of the particles are closed, and there is no suitable pore size for microbial adhesion and growth, which cannot improve the catalytic performance of the MCEs.

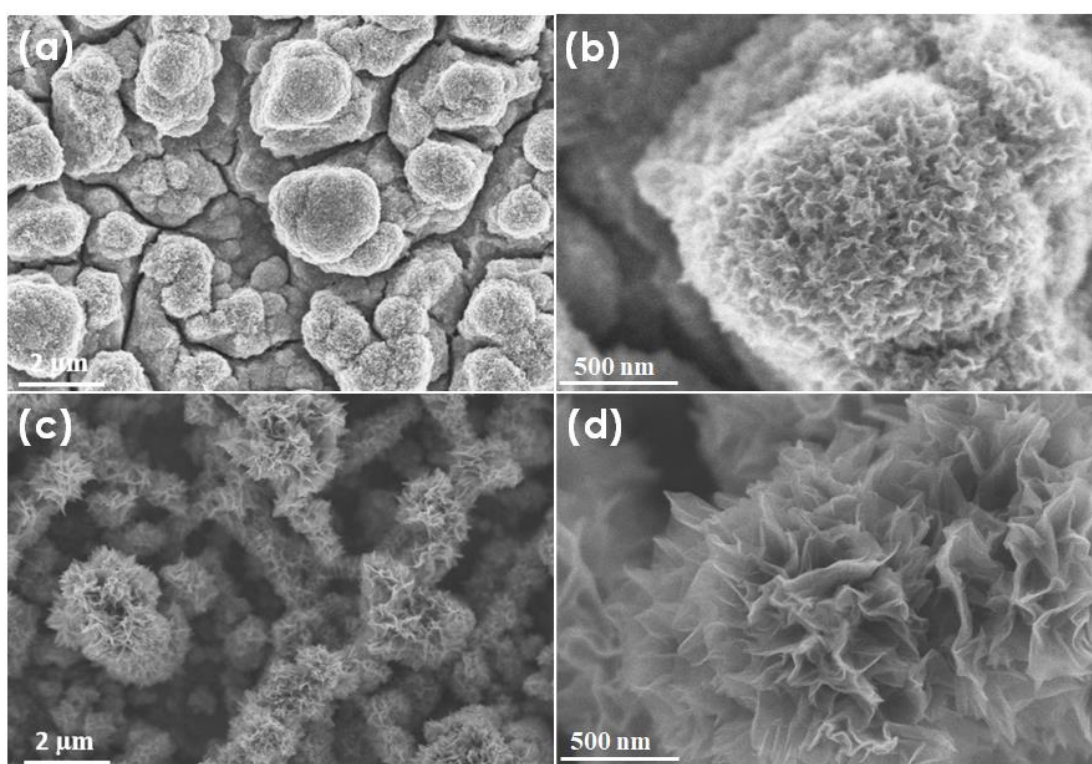


Figure 1. SEM images of (a, b) Mn_3O_4 and (c, d) $\text{rGO@Mn}_3\text{O}_4$.

The TEM of the Mn_3O_4 and $\text{rGO@Mn}_3\text{O}_4$ hybrid are rendered in Figure 2. As demonstrated in the Figure 2a and b, a pattern of light and dark suggests that the Mn_3O_4 particles show the tendency to aggregate, which is a negative sign for bacteria to attach and grow. However, highly dispersed Mn_3O_4 particles are uniformly formed on the rGO nanosheets during electrodeposition shown in the Figure 2c. As shown in the Figure 2d, the internal connections between the formed nanosheets in the hybrid material, which is beneficial to the establishment of electronic bridge in the electrode. The occurrence of C, O and Mn elements in the Figure S2 is consistent with the prediction, meanwhile the percentage of Mn element reached 63.78 %. And the element mappings correspond to the result of the EDX above, the C and O are homogeneity distributed in sheet layers (Figure 2c and d), Mn element shows a large corresponding to

the above two elements (Figure 2e and f), serving as a medium for the super match between the electrode materials and microbes [40].

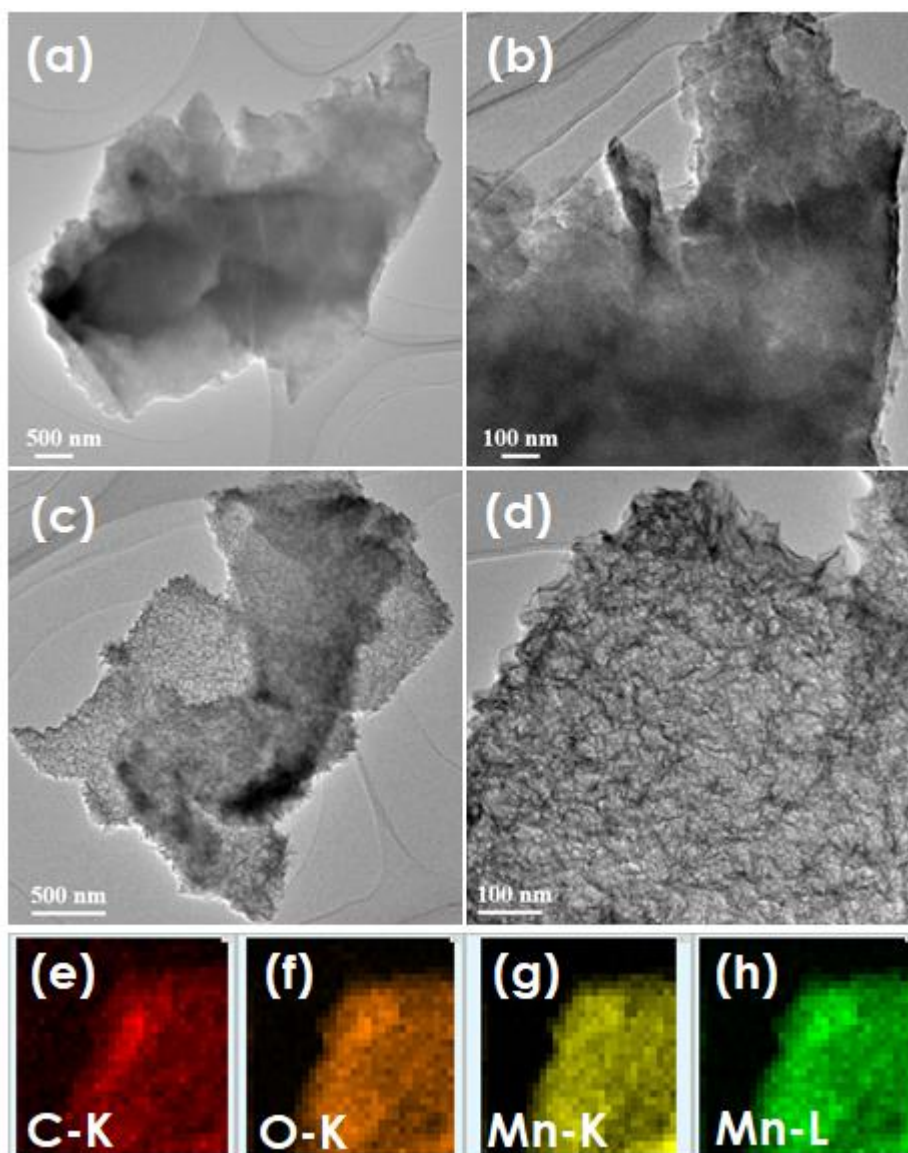


Figure 2. TEM images of Mn_3O_4 (a, b) and $\text{rGO@Mn}_3\text{O}_4$ (c, d); Corresponding elemental mapping of C (e), O (f) and Mn (g, h).

The construction of as-prepared $\text{rGO@Mn}_3\text{O}_4$ electrode was proved by Raman spectrum, as well as rGO and Mn_3O_4 . As shown in Figure 3a, the two characteristic peaks of 1346 cm^{-1} and 1600 cm^{-1} are attributed to the D and G bands of the rGO , respectively. The D/G band ratio for rGO is 0.985. The D band corresponds to the structural defects, while the G band is rated to the E_{2g} mode of sp^2 carbon. For the $\text{rGO@Mn}_3\text{O}_4$, the original characteristic peaks of rGO decreased significantly and shifted, and the new peaks of 568 cm^{-1} and 638 cm^{-1} appeared, almost corresponding to the peaks in the Mn_3O_4 curve, which might derive from the crystalline nanometer Mn_3O_4 [39, 41]. This indicates that the Mn_3O_4

particles are efficiently distributed on rGO flakes, may be the key to the colonization of microorganisms on the electrode and the formation of electronic transmission network. XPS measurements further comprehend the chemical properties and composition of rGO@Mn₃O₄ hybrid electrode. Figure 3b shows the wide-scan XPS spectrum of rGO@Mn₃O₄, which consists of the feature peaks for C, O and Mn, indicating that the large area load of Mn₃O₄ particles on rGO. The change of Mn oxidation state is shown in the Figure 3c and d, the Mn 2p and 3s in rGO@Mn₃O₄ hybrid material was analyzed. Mn 2p_{3/2} and Mn 2p_{1/2} correspond to peaks at 642.2 and 653.9 eV, respectively. The binding energies corresponding to the oxidation states of Mn (II) and Mn (III) are difficult to distinguish. Among these peaks, there is an 11.7 eV energy separation, which is consistent with the mixed valence Mn₃O₄ [42]. Two peaks of 83.7 and 89.3 eV were observed showing a separation of 5.6 eV, is rated to the mixed valence states formed from Mn (II) and Mn (III) [43]. And between the electrons in the Mn 3s and unpaired free electrons exists an exchange interaction, which leads to a splitting of the 3s spectrum, consistent with previous reports [44].

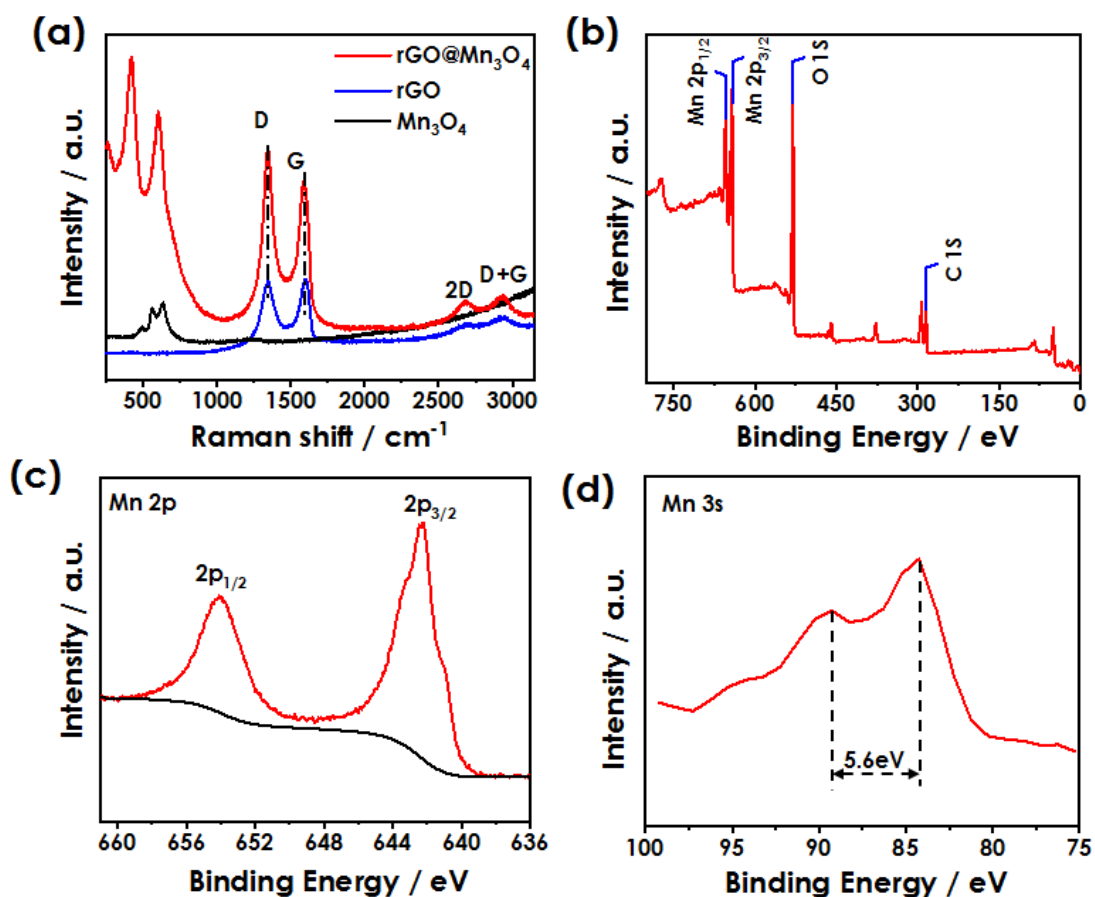


Figure 3. Raman spectrum of rGO, Mn₃O₄ and rGO@Mn₃O₄ (a); XPS pattern of rGO@Mn₃O₄ hybrid: (b) The survey scan spectrum of rGO@Mn₃O₄, (c) Mn 2p, (d) Mn 3s.

3.2 Electrochemical measurements

The electron transfer kinetics between the different electrodes were explored with electrochemical impedance spectroscopy (EIS). The well-defined single semicircle can be observed in the high frequency region, and the short line appears in the low frequency region in the Figure 4a. The diameter of the semicircle in the typical Nyquist plots is related to the variable transfer resistance (R_{ct}), which usually denotes the electrochemical resistance of the electrodes, and the smaller R_{ct} , the faster electron-transfer rate [45]. From the Figure 4a, we can notice that the semi-diameter of rGO@Mn₃O₄ is slightly larger than rGO, but much smaller than the semicircle diameter of the Mn₃O₄ electrode. From the above characterization results, it can be observed that Mn₃O₄ particles distributed on the rGO sheets with a high coverage. Due to the poor conductivity of Mn₃O₄, the electrochemical performance of the rGO@Mn₃O₄. Nevertheless, the hybridization still maintained excellent conductivity, implying that the interaction between rGO and Mn₃O₄ facilitates the transfer of electrons, which suggests that the rGO@Mn₃O₄ is the ideal conductive material for enhancing the microbial electron transfer [46].

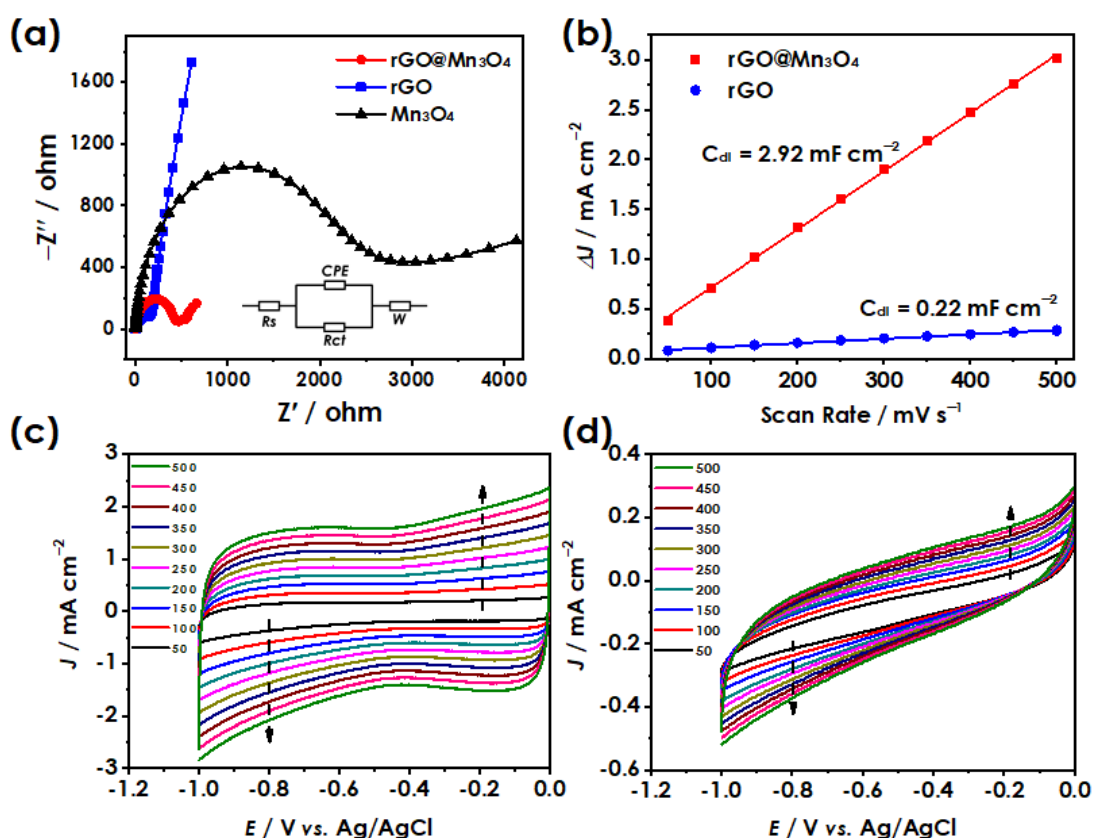


Figure 4. (a) Nyquist plots for rGO@Mn₃O₄, Mn₃O₄ and rGO modified electrodes measured over a frequency range of 0.01–100000 Hz with an AC perturbation of 5.0 mV at open circuit potential; (b) The capacitive current measured at -0.5 V vs. saturated Ag/AgCl was plotted as a function of scan rate; Cyclic voltammetry curves of rGO@Mn₃O₄ (c) and rGO (d) with different scan rates in N₂-saturated 1.0 M KCl solution.

Considering the induction behavior, the inert of Figure 4a shows the equivalent circuit, the solution of R_s is resistance, the charge transfer resistance is represented by R_{ct} , the CPE corresponds to

the double-layer capacitor and the electronic element on the rGO@Mn₃O₄ hybrid bioelectrode surface, and W is the finite layer diffusion impedance of the planar electrode [47]. The correlation between density of capacitive current and the scan rate of CV for the rGO and rGO@Mn₃O₄ is shown in Figure 4b, which is quasi-linear. Obviously, the slope value of I/V line of rGO@Mn₃O₄ hybrid electrode is much higher than the rGO. And the specific capacitance of the rGO@Mn₃O₄ is 2.29 mF cm⁻², which is much larger than 0.22 mF cm⁻² (rGO).

The electrochemical surface area (ECSA) was analyzed by CV technology. Figure 4c and d shows the cyclic voltammograms of rGO@Mn₃O₄, and rGO in the N₂-saturated 1.0 M KCl solution with the scan rate of 50 mV s⁻¹. All voltammetry diagrams exhibit a quasi-rectangular shape on account of the electricity double-layer capacitance. In addition, the maximal area of CV curve was obtained in the rGO@Mn₃O₄ hybrid, which demonstrates that the ECSA value of the rGO@Mn₃O₄ hybrid is much larger than that of rGO. In addition, as the scan rate of electrode potential increased (50-500 mV s⁻¹), the CV integral area and the ECSAs value of rGO@Mn₃O₄ and rGO become larger and higher from Figure 4c and d.

3.3 Microbial electrocatalytic performance

The output performance of the rGO@Mn₃O₄ hybrid as electrode was evaluated in the single-chamber BESs inoculated with *Geobacter*, meanwhile the rGO and Mn₃O₄ under the same battery structure and operating conditions have been investigated for comparison. As shown in Figure 5a, the rGO@Mn₃O₄ microbial electrode slowly increases to a stable shock region of 0.0375 mA cm⁻² for about 1.5 days, and then declines because of the consumption of sodium acetate. The electron generation activation and microbial colonization take place for cells on the hybrid electrode surface during this period. After supplementing sodium acetate, the cell voltage reached another higher stable plateau value of 0.0471 mA cm⁻², and then decreased again. The current density increased to the maximum of 0.0388 mA cm⁻², and the maximum current stable region (0.0388 ± 0.00435 mA cm⁻²) was maintained for 1 day, after the system was further replenished with sodium acetate. As for the cases of rGO and Mn₃O₄ structures in the Figure 5a, the BESs show maximum current maximum current about 0.0124 mA cm⁻² and 0.0070 mA cm⁻² respectively, and kept for 1 day, which are much lower than that of rGO@Mn₃O₄ electrode. These results can be naturally associated with that the rGO@Mn₃O₄ hybrid electrode producing more energy, while adding the same sufficient sodium acetate. At a consequence, the rGO@Mn₃O₄ hybrid shows unique scaffold, providing appropriate pore size and large specific area, which enable the bacteria to immobilize and grow in large quantities on bioelectrode, and to facilitate the nutrients diffusion from the overall solution to the interior of the electrode [48, 49]. The LSV curves shown in the Figure 5b, the rate of ascent and the current density of rGO@Mn₃O₄ are superior to rGO and Mn₃O₄. CV curves of rGO@Mn₃O₄, rGO and Mn₃O₄ bioelectrodes were also demonstrated in the Figure 5c, the result was consistent with the results based on LSV, which further confirmed the absolute advantage of rGO@Mn₃O₄ electrodes in conductivity [50].

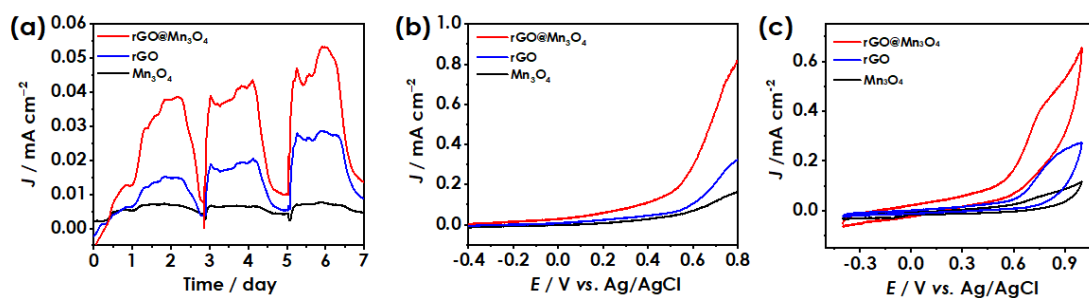


Figure 5. (a) Variation of current density over time for rGO@Mn₃O₄, Mn₃O₄ and rGO bioelectrodes polarized at 0 V vs. saturated Ag/AgCl (the arrows indicate feeding of 1.0 g L⁻¹ sodium acetate); (b) Linear cyclic voltammetry curves for rGO@Mn₃O₄, Mn₃O₄ and rGO bioelectrodes at a scan rate of 1.0 mV s⁻¹. (c) Cyclic voltammetry curves for rGO@Mn₃O₄, Mn₃O₄ and rGO bioelectrodes (scan rate 1.0 mV s⁻¹).

3.4 Biofilm morphology

For a reasonable explanation for the remarkable performance of the rGO@Mn₃O₄ bioelectrode, the SEM was employed to characterize the surface microtopography of three different microbial electrodes under 9 days operation. An interconnected and thick biofilm network is shown in Figure 6a, formed by *Geobacter* adhering to the scaffolds of the rGO@Mn₃O₄ electrode, indicating a favorable host and colonization structure for the *Geobacter*. On contrast, there is a trend of separation for biofilm on substrates in Figure 6c due to the excessively macroscale porous structure of Mn₃O₄, and a low density *Geobacter* distributed on the nanosheets in Figure 6e, owing to the of inherent flat structure of rGO. From the enlarge Figure 6b, many microbial nanowires (pill) are evident (such as those circled by a red dotted line), tethering cells to each other in a stable multi-layered network. Nevertheless, the microbial nanowires (pill) appear on the rGO and Mn₃O₄ electrodes far less compared to that of the rGO@Mn₃O₄ electrode in Figure 6d and f. According the previous studies, the nanowires (pill) might be the conductive bridges to make a connection between exoelectrogens and electrode materials [51-53]. This illustrates that the rGO@Mn₃O₄ scaffold possesses an appropriate high active surface area, which is conducive to the growth of biofilms and the formation of nanowires, thus facilitating the transfer of extracellular electrons in electrochemical reactions and providing more power density.

Based on the above discussion, rGO@Mn₃O₄ possesses open macroscale porous structure, which provides a large specific surface area. Meanwhile, the Mn₃O₄ particles coating improves both bioelectrocatalytic activity and electrode biocompatibility. Consequently, the rGO@Mn₃O₄ electrode enhances bacterial adhesion and electron transfer efficiency in the internal cell with a significant effect, resulting in a higher BESs performance.

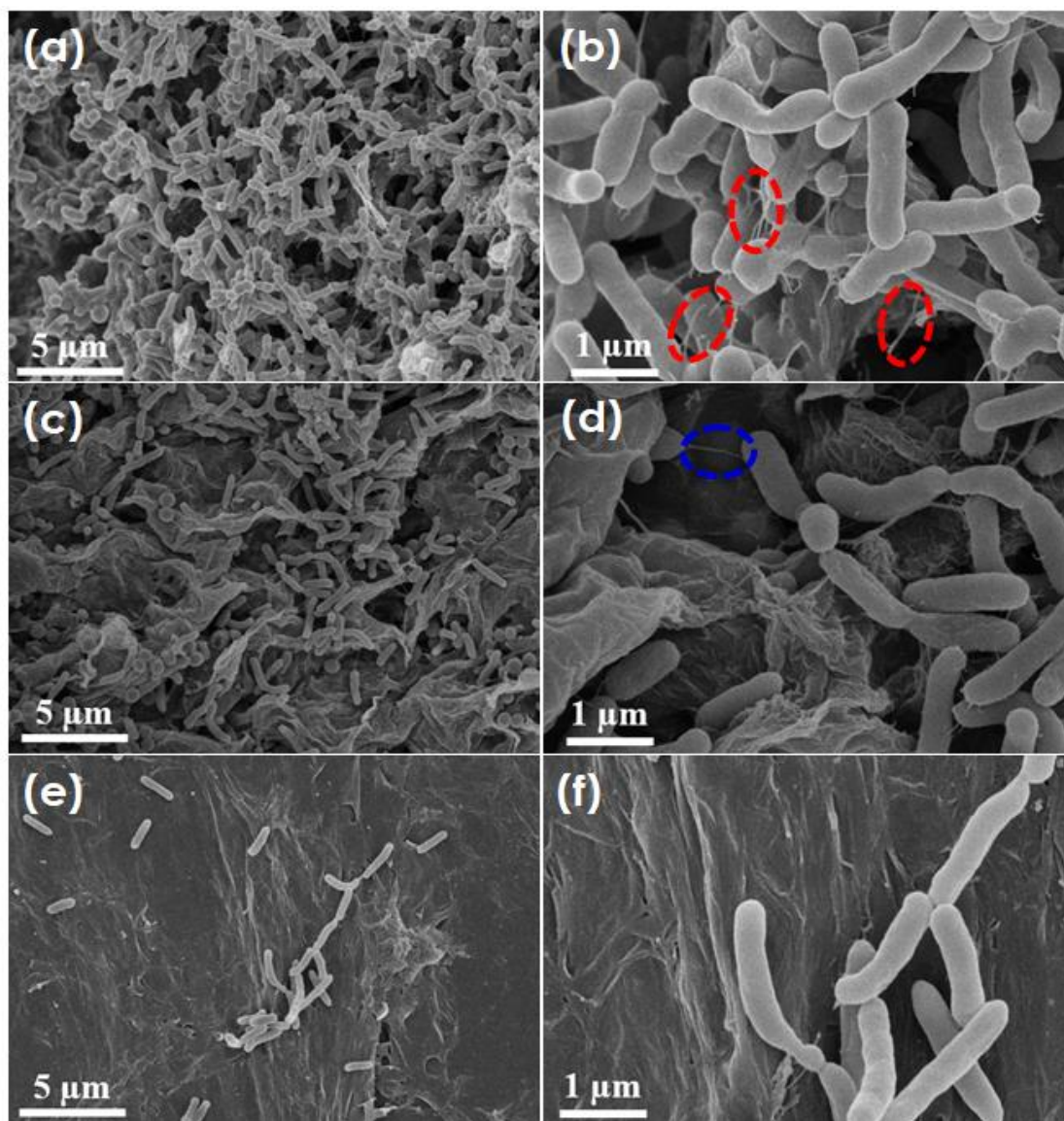


Figure 6. SEM images of the microbial growth on different materials: (a, b) rGO@Mn₃O₄; (c, d) Mn₃O₄ and (e, f) rGO.

4. CONCLUSIONS

In summary, we have successfully prepared hierarchically rGO@Mn₃O₄ nanostructured bioelectrode through one-step cyclic voltammetric electrodeposition, which shows excellent maximum power output in the *Geobacter*-catalyzed BESs. The obtained rGO@Mn₃O₄-*Geobacter sulfurreducens* bioelectrode resulted in highly efficient microbial electrocatalysis. The maximum current density achieved with the rGO@Mn₃O₄ electrode in a three-electrode setup was 0.0376 mA cm⁻², which is 3.03-fold higher than that of bare rGO (0.0124 mA cm⁻²), the favorable output property in BESs can be attributed to the optimal size matching of hierarchical pore structure between electrode nanomaterials and electrogenic microorganisms. In addition, high conductivity and great biocompatibility are realized at the same time through a “rose”-like structure Mn₃O₄ coating on the surface of the rGO sheets network,

which facilitate electron transfer and microbial attachment. This work demonstrates a high-performance bioelectrode material for BESs, providing a brand new insight on the bioelectrode design in microbial electrochemical systems.

ACKNOWLEDGEMENT

This study was financially supported by the National Key Research and Development Program of China (Nos. 2018YFC0406400 and 2019YFC1907900), the Key Science and Technology Projects of Inner Mongolia Autonomous Region (2019ZD001), the National Science Foundation of China (Nos. 51678285 and 51808279), the Key Project of Innovative Talents of Science and Technology of Jiangxi Province (No. 20181BCB18002), and the Fostering Project of National Science and Technology Awards of Jiangxi Province (No. 20192AEI91001).

SUPPORTING DATA

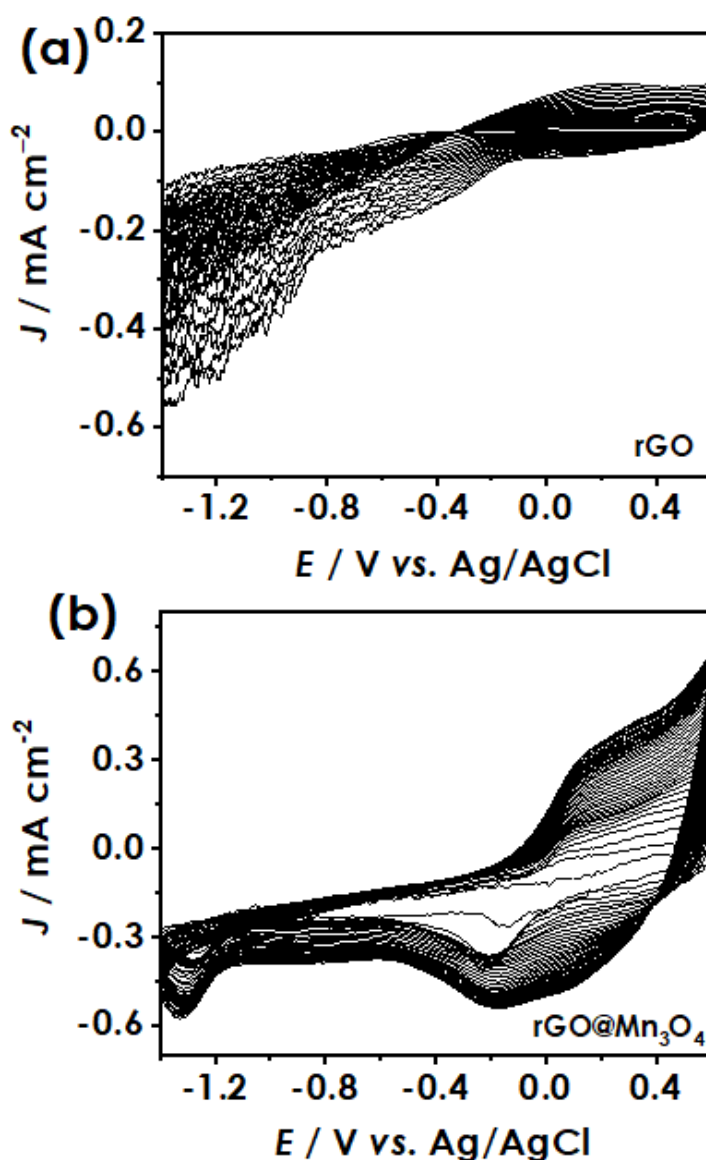


Figure S1. Cyclic voltammograms of the electrodeposition process for preparation of (a) rGO, (b) rGO@Mn₃O₄.

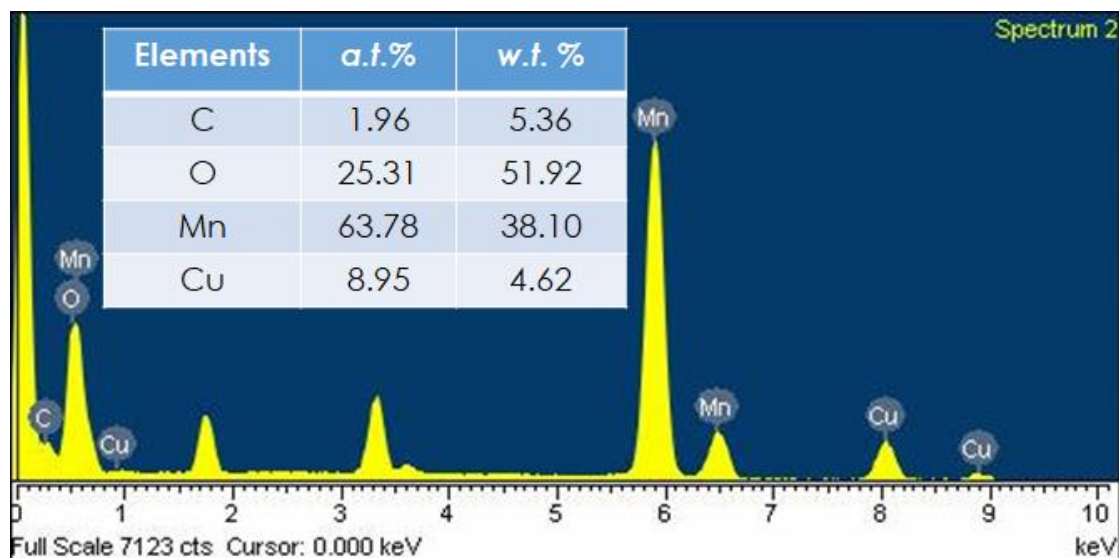


Figure S2. EDX of rGO@Mn₃O₄ hybrid and corresponding element content.

References

1. Y. K. Zhang, Z. S. Xiong, L. M. Yang, Z. Ren, P. H. Shao, H. Shi, X. Xiao, S. G. Pavlostathis, L. L. Fang, X. B. Luo, *Water Res.*, 166 (2019) 115076.
2. X. D. Ma, B. Liang, M. Y. Qi, H. Yun, K. Shi, Z. L. Li, Y. Q. Guo, P. S. Yan, S.-J. Liu, A. J. Wang, *Environ. Sci. Technol.*, 54 (2020) 7591–7600.
3. P. H. Shao, D. H. Liang, L. M. Yang, H. Shi, Z. S. Xiong, L. Ding, X. C. Yin, K. Zhang, X. B. Luo, *J. Hazard. Mater.*, 387 (2020) 121676.
4. W. Q. Lai, K. Zhang, P. H. Shao, L. M. Yang, L. Ding, S. G. Pavlostathis, H. Shi, L. Z. Zou, D. H. Liang, X. B. Luo, *J. Hazard. Mater.*, 379 (2019) 120791.
5. X. C. Yin, P. H. Shao, L. Ding, Y. Xi, K. Zhang, L. M. Yang, H. Shi, X. B. Luo, *Environ. Sci.: Nano*, 6 (2019) 3307–3315.
6. P. H. Shao, S. P. Yu, X. G. Duan, L. M. Yang, H. Shi, L. Ding, J. Y. Tian, L. X. Yang, X. B. Luo, S. B. Wang, *Environ. Sci. Technol.*, 54 (2020) 8464–8472.
7. L. M. Yang, G. P. Yi, Y. N. Hou, H. Y. Cheng, X. B. Luo, S. G. Pavlostathis, S. L. Luo, A. J. Wang, *Biosensors Bioelectron.*, 141 (2019) 111444.
8. X.-Q. Lin, Z.-L. Li, Bin Liang, H.-L. Zhai, W.-W. Cai, J. Nan, A.-J. Wang, *Water Res.*, 162 (2019) 236–245.
9. B. E. Logan, B. Hamelers, R. Rozendal, U. Schröder, J. Keller, S. Freguia, P. Aelterman, W. Verstraete, K. Rabaey, *Environ. Sci. Tech.*, 40 (2006) 5181–5192.
10. K. P. Katuri, S. Kalathil, A. Ragab, B. Bian, M. F. Alqahtani, D. Pant, P. E. Saikaly, *Adv. Mater.*, 30 (2018) 1707072.
11. R. Kumar, L. Singh, A. W. Zularisam, *Renew. Sustain. Energy Rev.*, 56 (2016) 1322–1336.
12. L. M. Yang, D. F. Yan, C. B. Liu, H. J. Song, Y. H. Tang, S. L. Luo, M. J. Liu, *J. Power Sources*, 278 (2015) 725–732.
13. S. Li, C. Cheng, A. Thomas, *Adv. Mater.*, 29 (2017) 1602547.
14. S. K. Chaudhury, D. R. Lovley, *Nat. Biotechnol.*, 21 (2003) 1229–1232
15. Y.-C. Yong, X.-C. Dong, M. B. Chan-Park, H. Song, P. Chen, *ACS Nano*, 6 (2012) 2394–2400.
16. Z. He, J. Liu, Y. Qiao, C. M. Li, T. T. Y. Tan, *Nano Lett.*, 12 (2012) 4738–4741.
17. X. Xie, G. Yu, N. Liu, Z. Bao, C. S. Criddle, Y. Cui, *Energy Environ. Sci.*, 5 (2012) 6862–6866.
18. J. Liu, Y. Qiao, C.X. Guo, S. Lim, H. Song, C.M. Li, *Bioresour. Technol.*, 114 (2012) 275–280.
19. Y. Z. Zhang, G. Q. Mo, X. W. Li, W. D. Zhang, J. Q. Zhang, J. S. Ye, X. D. Huang, C. Z. Yu, *J. Power Sources*, 196 (2011) 5402–5407.
20. L. Xiao, J. Damien, J. Y. Luo, H. D. Jang, J. X. Huang, Z. He, *J. Power Sources*, 208 (2012) 187–

192.

21. D. Li, M. B. Müller, S. Gilje, R. B. Kaner, G. G. Wallace, *Nat. Nanotechnol.*, 3 (2008) 101-105.
22. Y. C. Si, E. T. Samulski, *Nano Lett.*, 8 (2008) 1679-1682.
23. C. Shan, H. Yang, D. Han, Q. Zhang, A. Ivaska, L. Niu, *Langmuir*, 25 (2009) 12030-12033.
24. S. Z. Zu, B. H. Han, *J. Phys. Chem. C*, 113 (2009) 13651-13657.
25. J. W. T. Seo, A. A. Green, A. L. Antaris, M. C. Hersam, *J. Phys. Chem. Lett.*, 2 (2011) 1004-1008.
26. Y. C. Si, E. T. Samulsk, *Chem. Mater.*, 20 (2008) 6792-6797.
27. C. Xu, F. Kang, B. Li, H. Du, *J. Mater. Res.*, 25 (2011)1421-1432.
28. W. Wei, X. Cui, W. Chen, D. G. Ivey, *Chem. Soc. Rev.*, 40 (2011) 1697-1721.
29. X. J. Yang, Y. J. Makita, Z. H. Liu, K. H. Sakane, K. Ooi, *Chem. Mater.*, 16 (2004) 5581-5588.
30. C. Y. Zhang, P. Liang, X. F. Yang, Y. Jiang, Y. H. Bian, C. M. Chen, X. Y. Zhang, X. Huang, *ACS Appl. Mater. Inter.*, 81 (2016) 32-38.
31. Y. Wang, L. Cheng, F. Li, H. Xiong, Y. Xia, *Chem. Mater.*, 19 (2017) 2095-2101.
32. L. Mao, D. Zhang, T. Sotomura, K. Nakatsu, N. Koshiba, T. Ohsaka, *Electrochim. Acta*, 48 (2003) 1015-1021.
33. L. Mao, T. Sotomura, K. Nakatsu, N. Koshiba, D. Zhang, T. J. Ohsaka, *Electrochem. Soc.*, 149 (2002) A504-A507.
34. Y. Gorlin, C. J. Chung, D. Nordlund, B. M. Clemens, T. F. Jaramillo, *ACS Catal.*, 2 (2012) 2687-2694.
35. F. Cheng, J. Shen, W. Ji, Z. Tao, J. Chen, *ACS Appl. Mater. Inter.*, 1 (2009) 460-466.
36. G. P. Yi, Z. W. Chang, G.Z. Liu, L. M. Yang, *Int. J. Electrochem. Sci.*, 14 (2019) 7232-7240.
37. L. M. Yang, D. F. Yan, C. B. Liu, H. J. Song, Y. H. Tang, S. L. Luo, M. J. Liu, *J. Power Sources*, 278 (2015) 725-732.
38. Y. N. Hou, H. Liu, J. L. Han, W. W. Cai, J. Z. Zhou, A. J. Wang, H. Y. Cheng, *ACS Sustain. Chem. Eng.*, 4 (2016) 5392-5397.
39. G. Reguera, K. D. McCarthy, T. Mehta, J. S. Nicoll, M. T. Tuominen, D. R. Lovley, *Nature*, 435 (2005) 1098-1101.
40. B. Sourav, R. Kanak, S. Chinnakonda, C. Gopinath, R. Retna, *ACS Appl. Mater. Inter.*, 6 (2014) 2692-2699.
41. B. E. Logan, K. Rabaey, *Science*, 337 (2012) 686-690.
42. B. Murugan, D. Srinivas, C. S. Gopinath, V. Ramaswamy, A. V. Ramaswamy, *Chem. Mater.*, 17 (2015) 3983-3993.
43. V. L. J. Joly, P. A. Joy, S. K. Date, C. S. Gopinath, *Phys. Rev. B.*, 65 (2002) 184416.
44. J. W. Lee, A. S. Hall, J. D. Kim, T. E. Mallouk, *Chem. Mater.*, 24 (2012) 1158-1164.
45. M. Huang, Y. Zhang, F. Li, L. Zhang, R. S. Ruoff, Z. Wen, Q. Liu, *Surf. Sci. Rep.*, 4 (2014) 3878.
46. A. Ejigu, M. Edwards, D. A. Walsh, *ACS Catal.*, 5 (2015) 7122-7130.
47. A. Safavi, H. Kazemi, S. H. Kazemi, *J. Power Sources*, 256 (2014) 354-360.
48. L. Deng, S. Guo, Z. Liu, M. Zhou, D. Li, L. Liu, G. Li, E. Wang, S. Dong, *Chem. Commun.*, 46 (2010) 7172-7174.
49. L. Peng, S.-J. You, J.-Y. Wang, *Biosens. Bioelectron.*, 25 (2010) 1248-1251.
50. Y. Lin, P. Ning, Y. Cui, C. Zhang, M. Xu, P. Dong, Z. Zhou, Y. Zhang, *Int. J. Electrochem. Sci.*, 14 (2019) 4003-4019.
51. Y. Qiao, C. M. Li, S. J. Bao, Q. L. Bao, *J. Power Sources*, 170 (2007) 79-84.
52. T. Q. Lin, I.-W. Chen, F. X. Lin, C. Y. Yang, H. Bi, F. F. Xu, F. Q. Huang, *Science*, 350 (2015) 1508.
53. T. Zhang, Y. Zeng, S. Chen, X. Ai, H. Yang, H. *Electrochem. Commun.*, 9 (2007) 349-353.